Supporting Information for

First-row transition elements in pyroxenites and peridotites: a promising tool for constraining mantle source mineralogy.

O. I. Lang & S. Lambart
The University of Utah, Department of Geology and Geophysics, MagMaX Laboratory.

Contents of this file: Supplementary Texts S1 to S4, Figures S1 to S11, Tables S3 and S7, and the list of references cited in the supportive information.

Additional Supporting Information (Files uploaded separately):

Table S1. EarthChem compilation of minerals from pyroxenites used in this study.
Table S2. EarthChem compilation of minerals from peridotites used in this study
Table S4. Average concentrations in minerals from pyroxenite samples obtained with microprobe analyses.
Table S5. Average trace element concentrations in minerals from San Carlos xenoliths
Table S6. Trace elements analyses (LA-ICP-MS) in individual grains from San Carlos xenoliths

Text S1: FRTE crystallographic distribution

S1.1 Olivine and orthopyroxene

As a common constituent in mafic and ultramafic rocks worldwide, olivine takes on the general end-member formula Mg_2SiO_4 (forsterite), with Mg^{2+} indiscernibly occupying two octahedral crystallographic sites, M1 and M2. Because of ionic radii comparable to Mg^{2+} in 6-fold coordination, Ni^{2+}, Co^{2+}, Zn^{2+}, Mn^{2+} and Fe^{2+} can substitute for Mg^{2+} in both M1 and M2 octahedral sites. Cr^{3+}, V^{3+}, Sc^{3+}, however, are usually occupy the slightly smaller M1 sites (e.g., Papike *et al.,* 2005). Finally, Ti^{4+} is much smaller and preferentially substitutes for Si^{4+} in tetrahedral sites in anhydrous olivine. It can also be incorporated into M1 sites under hydrous conditions (Cherniak & Liang, 2014, and references therein).

The Mg end-member formula for orthopyroxene is $MgSiO_3$ (enstatite). As in olivine, all of the metal cation sites are in 6-fold coordination. Hence, FRTEs are incorporated in a similar way in olivine and orthopyroxene. Ti^{4+} is preferentially incorporated into M1 sites (Papike et al., 2005).

S1.2 Clinopyroxene

As we will see in later sections, the vast majority of clinopyroxene analyses used in this paper are diopsidic and therefore take on the general end-member formula: $CaMgSi_2O_6$. Unlike olivine and orthopyroxene, in clinopyroxene, the M2 site (or X site), can either be in 8-fold coordination (when occupied by Ca, Na) or in distorted 6-fold coordination (when occupied by Mg) (e.g., Deer *et al.*, 1963; Le Roux *et al.,* 2010; Papike *et al.,* 2005). Since FRTEs preferentially occupy 6-fold over 8-fold coordination sites, their presence is not equally distributed between the two crystallographic sites.

S1.3 Garnet

The general formula of garnet is $X_3Y_2(SiO_4)_3$, with X sites representing large 8-fold coordination sites commonly occupied by divalent cations, and Y sites being 6-fold coordination sites mostly occupied by trivalent cations. Natural compositions of mantle garnets are usually in the range of pyrope ($Mg_3Al_2(SiO_4)_3$), almandine ($Fe_3Al_2(SiO_4)_3$), and uvarovite ($Ca_3Cr_2(SiO_4)_3$) (e.g., Deer *et al*., 1997). Scandium is incorporated in both the X and Y sites of Cr-Ca-rich garnets (e.g., Chassé *et al*., 2018). Other trivalent cations (Cr^{3+} and V^{3+}) and Ti^{4+} occupy the Y site (e.g., Ackerson *et al*., 2017). In particular, the partitioning of Cr between garnet and cpx is mostly controlled by composition. Cr is preferentially incorporated into grossular over jadeite, but is preferentially incorporated into jadeite over pyrope (Figowy *et al.,* 2020). This might explain the large error bars associated with $D_{Cr}^{gnt/cpx}$ calculated on natural samples (Fig. 6 in the manuscript).

S1.4 Spinel

The spinel group contains a very large array of different minerals, taking the general formula of AB_2O_4. Commonly, the A (octahedral) and B (tetrahedral) crystallographic site are filled with divalent and trivalent cations, respectively, although other combinations of cations are possible. Spinel end-members are grouped by their B crystallographic site. Common examples include the Al, Fe, and Cr series of spinel. The Al series (or Spinel series) can occur in Al-rich xenoliths. Both Fe and Zn commonly occur with Mg in the A site. Trace amounts of Cr are regularly found in the Al site. The Fe (or magnetite) series composes common oxide minerals in a variety of mafic and ultramafic rocks and can contain many FRTEs including Cu, Mn, Zn, Ti and Ni that can be the dominant chemical constituent or occur in trace abundance within the A crystallographic site. Similarly, the Cr (chromitite) series, most commonly found in cumulates associated with complexes of ultramafic rock, make contain Fe or Zn in its A sites.

S1.5 Effect of oxygen fugacity on the partitioning of multivalent cations between minerals.

Iron is the dominant multivalent cation on Earth. The importance of the Fe^{2+} to Fe^{3+} transition due to the increase of the oxygen fugacity (f_{O_2}) cannot be overstated since the Fe^{3+}-Al^{3+} substitution is of high importance in many geological processes (Papike et al., 2005). The implications of variable f_{O_2} on the outputs of the melting models are discussed in Text S2. Here we review the effect of f_{O_2} on the mineral-mineral partition behaviors of V, Ti and Cr.

Partition coefficients for V between olivine, orthopyroxene, clinopyroxene, spinel and garnet relative to silicate melt are strongly dependent on oxygen fugacity (Mallmann & O'Neill, 2009). For conditions relevant for the Earth (QFM ± 5, Mallmann *et al.,* 2021), all *Ds* decrease with increasing f_{O_2}. In particular, V partitions similarly into garnet and clinopyroxene (Holycross & Cottrell, 2022; Mallmann & O'Neill, 2009). Hence, despite a strong effect of the f_{O_2} on the partitioning of V between solid phases and silicate melt, the consistency in behavior across all solid mantle phases results in a very moderated effect of variable f_{O_2} on the $D_V^{mnl/mnl}$s.

The effect of variable f_{O_2} is more limited for other elements of variable valency states. The partition coefficients of Ti for olivine, orthopyroxene, and clinopyroxene with silicate melt decrease with increasing f_{O_2} up to QFM−2, above which the coefficient stays constant (Mallmann & O'Neill, 2009). Once again, the consistent behavior between minerals results in a negligible effect of f_{O_2} on $D_{Ti}^{mnl/cpx}$ (see Fig. 6 in the main manuscript). Oxygen fugacity has no direct effect on the partitioning of Ti in spinel, but $D_{Ti}^{sp/melt}$ strongly depends on composition and increases with Fe^{3+} content (Wijbrans *et al.,* 2015). Hence, an increase in oxygen fugacity (resulting in an increase of Fe^{3+}/Fe^{2+}) will results in an increase of $D_{Ti}^{sp/melt}$. Because other coefficients decrease or remain constant with increasing f_{O_2}, this could, in theory, result in larger range of $D_{Ti}^{sp/cpx}$ with variable f_{O_2}. However, the effect of oxygen fugacity is likely to be

negligeable in comparison to the effect of composition since the partitioning of Ti in spinel is mainly controlled by the nature of the trivalent cation (ie. Al^{3+} vs Cr^{3+}; Wijbrans *et al.,* 2015). The spinel Cr# (=Cr/(Cr+Al) in mol%) in pyroxenite and peridotite varies considerably (e.g., Laukert et al., 2014) and this variability is likely responsible for the large errors bars for $D_{Ti}^{sp/cpx}$ on natural samples observed in Fig. 6.

Finally, Cr tends to become increasingly compatible in pyroxenes (Mallmann & O'Neill, 2009) and garnet with increasing f_{O_2} while its partitioning behavior stays relatively constant in olivine. This might result in a change of $D_{Cr}^{ol/cpx}$ by one order of magnitude for the range of f_{O_2} on Earth. However, despite this variability, $D_{Cr}^{ol/cpx}$ stays well below 1 (Fig. 6 in the manuscript).

Text S2: Summary of the analytical methods.

S2.1. Mineralogy

To obtain the mineralogy of our samples (Table S1), we performed point-counting using the software Rock.AR (Larrea *et al.,* 2014). Rock.AR is a visualization tool designed to do point counting from petrographic thin sections. We used a grid of 100 columns which approximatively correspond to squares of 0.15 mm^2. For each square, we considered the dominant mineral as the mineral present.

S2.2. Electron microprobe analyses

We determined major and minor concentrations using an electron microprobe. Analyses were performed at the University of Utah using a Cameca SX100 and processed using the 'Probe for EPMA' software. We used the two-step analyses described in detail in Lambart *et al.* (2022) during which we first analyzed the major elements at 30 nA and 15 keV using a 5um spot; on-peak counting times ranged from 20 to 30s. In subsequent analytical sessions, Ni, Mn, and Zn were analyzed at 25 keV with a 300 nA beam and a 10 um spot and 90 to 120 s on peak. These new data were then processed using the other element concentrations from the low beam current analyses. During each analytical session, half of the on-peak time was used on each of the high and low backgrounds. BHVO-2g secondary standard was repeatedly analyzed during each analytical session to monitor drift on major elements (i.e., using 15 keV, 30 nA and a 10 µm spot), but no additional corrections were applied.

S2.3. LA-ICP-MS analyses

Analyses were performed at the University of Utah on a Teledyne-Photon Machines Analyte Excite Excimer Laser Ablation system attached to an Agilent 8900 ICP-MS. Details on the method are provided in Lambart et al. (2022). The laser fluence was set at 0.47 J/cm^2. The laser carrier and the nebulizer gas flow were 1 L He/min (0.4 L/min cup +0.6 L/min cell) and 1.1 L Ar/min, respectively. We performed two analyses per grain from the selected San Carlos

xenoliths to allow mineral compositional variability to be assessed. Analyses were acquired with lines of 300 µm. Beam diameter and sample translations rates were 80 µm and 12 µm/s, respectively. We used a laser operating at 10 Hz frequency and each analysis was preceded by a cleaning shot. Acquisition times were about 50s. LA-ICP-MS data were treated with Excel. We used the silicate glass standard NIST 610 for Ni and Mn and NIST 612 for all other elements as reference material. The Si contents, measured by electron microprobe, served as an internal standard. We tested the accuracy of the measurement with BCR-2G as an external standard with an analysis every 4 to 6 sample analyses. The relative errors on the trace element contents lie between 0.2 and 15% (see Table S2 in Lambart *et al.*, 2022).

Text S3: Experimental $\mathbf{K_{D_{FRTE}}^{min/cpx}}$

To calculate the experimental $K_{D_{FRTE}}^{min/cpx}$ reported in Table 1 in the manuscript, we used the recommended values of $D_{FRTE}^{min/melt}$ reported in Table 3 in Le Roux *et al.* (2015). This table combines multiple experimental studies performed at various pressure and temperature conditions and for various degrees of oxidation. An example of calculation is described below for $K_{D_{Mn/Fe}}^{ol/cpx}$ and its associated one standard deviation:

For low pressure (LP) experiments on spinel peridotite assemblage, the recommended values for $D_{Mn}^{ol/melt}$ and $D_{Mn}^{cpx/melt}$ are:

$D_{Mn}^{ol/melt} = 0.77 \pm 0.02$ and $D_{Mn}^{cpx/melt} = 1.11 \pm 0.05$

Hence, $D_{Mn}^{ol/cpx} = D_{Mn}^{ol/melt} / D_{Mn}^{cpxl/melt} = 0.694$

and the standard deviation (σ) on $D_{Mn}^{ol/cpx}$ can be calculated with equation:

$$\sigma\left(D_{Mn}^{ol/cpx}\right) = D_{Mn}^{ol/cpx} \sqrt{\left(\frac{\sigma\left(D_{Mn}^{ol/melt}\right)}{D_{Mn}^{ol/melt}}\right)^2 + \left(\frac{\sigma\left(D_{Mn}^{cpx/melt}\right)}{D_{Mn}^{cpx/melt}}\right)^2} = 0.036$$

We can do the same with Fe and determine $D_{Fe}^{ol/cpx} = 1.49 \pm 0.11$.

$K_{D_{Mn/Fe}}^{ol/cpx}$ is the ratio of both partition coefficients: $K_{D_{Mn/Fe}}^{ol/cpx} = D_{Mn}^{ol/cpx} / D_{Fe}^{ol/cpx} = 0.46$

and its standard deviation is:

$$\sigma_{LP}\left(K_{D_{Mn/Fe}}^{ol/cpx}\right) = K_{D_{Mn/Fe}}^{ol/cpx} \sqrt{\left(\frac{\sigma\left(D_{Mn}^{ol/cpx}\right)}{D_{Mn}^{ol/cpx}}\right)^2 + \left(\frac{\sigma\left(D_{Fe}^{ol/cpx}\right)}{D_{Fe}^{ol/cpx}}\right)^2} = 0.042$$

The same calculations are performed using melt-mineral partition coefficients from high pressure (HP) experiments on garnet peridotite.

Finally, the $K_{D_{Mn/Fe}}^{ol/cpx} = 0.47$ reported in Table 1 is the average between $K_{D_{Mn/Fe}}^{ol/cpx}$ for low- and high-pressure peridotite assemblages with the standard deviation being:

$$\sigma\left(K_{D_{Mn/Fe}}^{ol/cpx}\right)=\frac{\overline{K_{D_{Mn/Fe}}^{ol/cpx}}}{2}\sqrt{\left(\sigma_{LP}\left(\left(K_{D_{Mn/Fe}}^{ol/cpx}\right)_{LP}\right)\right)^2+\left(\sigma_{HP}\left(\left(K_{D_{Mn/Fe}}^{ol/cpx}\right)_{HP}\right)\right)^2}=0.02$$

The same process was repeated for $K_D^{opx/cpx}$. For $K_D^{gnt/cpx}$, we consider both the high-pressure garnet peridotite assemblages and the eclogitic assemblage. Finally, the $K_D^{sp/cpx}$ were derived from the recommended values for a spinel peridotite assemblage.

Text S4: Melt modeling

S4.1. Validity of the batch melting model

In Figure S8a, we compare the Mn/Fe ratio in a melt produced by pure peridotite melting and pure pyroxenite melting as a function of the melt fraction (F) obtained using the modal batch melting equation (7) and the following fractional melting equation:

$$(Mn/Fe)_{liq}=(Mn/Fe)_0*\frac{\left(\frac{1}{D_0^{Mn}}\right)\cdot(1-F)^{\left(\frac{1}{D_0^{Mn}}-1\right)}}{\left(\frac{1}{D_0^{Fe}}\right)\cdot(1-F)^{\left(\frac{1}{D_0^{Fe}}-1\right)}} \quad \text{(S1)},$$

We used the same mineral proportion as in the first run of section 6.3: the modal proportion of the peridotite is 53.1% ol, 27.3% opx, 17.7% cpx, 1.9% gt (that is, the subsolidus modal proportion of the peridotite KR4003 at 3 GPa; Walter, 1998); the modal proportion of the pyroxenite is 82% cpx and 18% gnt (i.e., the near-solidus modal proportion of the MORB-type eclogite G2 at 3 GPa; Pertermann & Hirschmann, 2003b). For the partition coefficients of Fe and Mn, we used the recommended values by Le Roux *et al.,* (2015). Calculated values are D_0^{Fe}=0.80 and 1.22, D_0^{Mn}=0.75 and 2.20, for the peridotite and the eclogite, respectively.

Up to ~50% melting, both equations produced very similar results for peridotite- and eclogite-derived melt, demonstrating that using batch melting does not significantly affect the calculations outputs. Results are also consistent with the experimental melts produced by the peridotite KR4003 (Walter, 1998) and the eclogite G2 (Pertermann & Hirschmann, 2003a).

In Figure 7b, we compare the results obtained with equation (S1) where we consider a constant bulk $(Mn/Fe)_0$ for both lithologies (Fig. S10) with considering a different value for each lithology. The EarthChem database produces ratios of (Mn/Fe) = $1.58*10^{-2}$ for the peridotite dataset and (Mn/Fe) = $2.03*10^{-2}$ for the pyroxenite dataset. Using these values in equation (S1) slightly reduces the difference between the melt ratios, but results in lowering both the peridotite-derived melt ratio and increasing the pyroxenite-derived melt ratio, therefore not necessarily affecting the calculated proportion of pyroxenite component in the melt. Additionally, the difference in the Zn/Fe ratio between natural peridotites and pyroxenites is even smaller (Fig. S10).

Finally, in all the considered models, the ratios in both peridotite and eclogite melts stay relatively constant for F between 0 and 20%.

S4.2. Effect of oxygen fugacity on the model outputs.

In both olivine and clinopyroxene, Fe^{3+} behaves as an incompatible element. However $D_{Fe3+}^{ol/melt} << D_{Fe3+}^{cpx/melt}$ and $D_{Fe3+}^{cpx/melt}$ increases with increasing f_{O_2} (Rudra & Hirschmann, 2022). Hence, the total Fe content in magma will increase with increasing f_{O_2}, but at a faster pace for olivine-dominated source (aka peridotites) than for pyroxene dominated source (aka pyroxenites). Hence, the oxygen fugacity of the mantle might affect the ratio of the Mn/Fe (or Zn/Fe) ratio in magmas, If the f_{O_2} is not constrained, this will result in additional uncertainty on the mineralogical proportions in the source. In future studies, the effect of f_{O_2} can be tested by other FRTEs ratios that are independent of the oxygen fugacity (e.g., Mn/Zn).

References.

Ackerson, M. R., Watson, E. B., Tailby, N. D., & Spear, F. S. (2017). Experimental investigation into the substitution mechanisms and solubility of Ti in garnet. American Mineralogist, 102(1), 158-172.

Beard, B. L., Medaris, L. G., Johnson, C. M., Brueckner, H. K., & Mísař, Z. (1992). Petrogenesis of Variscan high-temperature Group A eclogites from the Moldanubian Zone of the Bohemian Massif, Czechoslovakia. Contributions to Mineralogy and Petrology, 111(4), 468-483.

Bernard-Griffiths, J., Carpenter, M. S. N., Peucat, J. J., & Jahn, B. M. (1986). Geochemical and isotopic characteristics of blueschist facies rocks from the Ile de Groix, Armorican Massif (northwest France). Lithos, 19(3-4), 235-253.

Beunon, H., Mattielli, N., Doucet, L. S., Moine, B., & Debret, B. (2020). Mantle heterogeneity through Zn systematics in oceanic basalts: Evidence for a deep carbon cycling. Earth-Science Reviews 205, 103-174.

Brey, G. P., & Köhler, T. (1990). Geothermobarometry in four-phase lherzolites II. New thermobarometers, and practical assessment of existing thermobarometers. Journal of Petrology, 31(6), 1353-1378.

Chassé, M., Griffin, W. L., Alard, O., O'reilly, S. Y., & Calas, G. (2018). Insights into the mantle geochemistry of scandium from a meta-analysis of garnet data. Lithos, 310, 409-421.

Cherniak, D. J., & Liang, Y. (2014). Titanium diffusion in olivine. Geochimica et Cosmochimica Acta, 147, 43-57.

Davis, F. A., Humayun, M., Hirschmann, M. M., & Cooper, R. S. (2013). Experimentally determined mineral/melt partitioning of first-row transition elements (FRTE) during partial melting of peridotite at 3 GPa. *Geochimica et Cosmochimica Acta* 104, 232-260.

Deer, W. A., Howie, R. A., & Zussman, J. (1963). Rock-Forming Minerals, Volume 2: Chain Silicates. *Longmans*, London, pp. 379.

Deer, W. A., Howie, R. A., & Zussman, J. (1997). Rock-Forming Minerals vol. 1A: Orthosilicates (second edition). *The Geological Society*, London, pp. 932.

Eason, D. E., Sinton, J. M., Grönvold, K., & Kurz, M. D. (2015). Effects of deglaciation on the petrology and eruptive history of the Western Volcanic Zone, Iceland. Bulletin of Volcanology 77, 1-27.

Figowy, S., Dubacq, B., Noel, Y., & d'Arco, P. (2020). Partitioning of chromium between garnet and clinopyroxene: first-principle modelling versus metamorphic assemblages. European Journal of Mineralogy, 32(4), 387-403.

Hills, D. V., & Haggerty, S. E. (1989). Petrochemistry of eclogites from the Koidu kimberlite complex, Sierra Leone. Contributions to Mineralogy and Petrology, 103(4), 397-422.

Holycross, M., & Cottrell, E. (2022). Experimental quantification of vanadium partitioning between eclogitic minerals (garnet, clinopyroxene, rutile) and silicate melt as a function of temperature and oxygen fugacity. Contributions to Mineralogy and Petrology, 177(2), 1-23.

Kimura, J. I., & Kawabata, H. (2015). Ocean Basalt Simulator version 1 (OBS 1): Trace element mass balance in adiabatic melting of a pyroxenite-bearing peridotite. Geochemistry, Geophysics, Geosystems, 16(1), 267-300.

Koornneef, J. M., Stracke, A., Bourdon, B., Meier, M. A., Jochum, K. P., Stoll, B., & Grönvold, K. (2012). Melting of a two-component source beneath Iceland. Journal of Petrology, 53(1), 127-157.

Lambart. S., Hamilton, S. & Lang, O. I. (2022) Compositional variability of San Carlos olivine. Accepted in Chemical Geology. doi: 10.1016/j.chemgeo.2022.120968

Larrea, M. L., Castro, S. M., & Bjerg, E. A. (2014). A software solution for point counting. Petrographic thin section analysis as a case study. Arabian Journal of Geosciences, 7(8), 2981-2989.

Laukert, G., Von Der Handt, A., Hellebrand, E., Snow, J. E., Hoppe, P., & Klügel, A. (2014). High-pressure reactive melt stagnation recorded in abyssal pyroxenites from the ultraslow-spreading Lena Trough, Arctic Ocean. Journal of Petrology, 55(2), 427-458.

Le Roux, V., Dasgupta, R., & Lee, C. T. A. (2015). Recommended mineral-melt partition coefficients for FRTEs (Cu), Ga, and Ge during mantle melting. American Mineralogist 100, 2533-2544.

Le Roux, V., Lee, C. T., & Turner, S. J. (2010). Zn/Fe systematics in mafic and ultramafic systems: Implications for detecting major element heterogeneities in the Earth's mantle. Geochimica et Cosmochimica Acta 74, 2779-2796.

Mallik, A., Lambart, S., & Chin, E. J. (2021). Tracking the evolution of magmas from heterogeneous mantle sources to eruption. In: Konter J., Ballmer M, Cottaar S, & Marquardt H. (Eds.), Mantle Convection and Surface Expressions. Geophysical Monograph 263, pp. 153-176, doi:10.1002/9781119528609.ch6.

Mallmann, G., & O'Neill, H. S. C. (2009). The crystal/melt partitioning of V during mantle melting as a function of oxygen fugacity compared with some other elements (Al, P, Ca, Sc, Ti, Cr, Fe, Ga, Y, Zr and Nb). Journal of Petrology, 50(9), 1765-1794.

Mallmann, G., Burnham, A. D., & Fonseca, R. O. (2021). Mineral-Melt Partitioning of Redox-Sensitive Elements. Magma Redox Geochemistry, 345-367.

Miller, C., & Stosch, H. G. (1988). Geochemistry and origin of eclogites from the type locality Koralpe and Saualpe, Eastern Alps, Austria. Chemical Geology, 67(1-2), 103-118.

Papike, J. J., Karner, J. M., & Shearer, C. K. (2005). Comparative planetary mineralogy: Valence state partitioning of Cr, Fe, Ti, and V among crystallographic sites in olivine, pyroxene, and spinel from planetary basalts. American Mineralogist, 90(2-3), 277-290.

Pertermann, M., & Hirschmann, M. M. (2003a). Anhydrous partial melting experiments on MORB-like eclogite: phase relations, phase compositions and mineral–melt partitioning of major elements at 2–3 GPa. Journal of Petrology 44, 2173-2201.

Pertermann, M., & Hirschmann, M. M. (2003b). Partial melting experiments on a MORB-like pyroxenite between 2 and 3 GPa: Constraints on the presence of pyroxenite in basalt source regions from solidus location and melting rate. Journal of Geophysical Research: Solid Earth, 108(B2).

Ravna, K. (2000). The garnet–clinopyroxene Fe2+-Mg geothermometer: an updated calibration. Journal of Metamorphic Geology 18, 211-219.

Rudra, A., & Hirschmann, M. M. (2022). Fe3+ partitioning between clinopyroxene and silicate melt at 1–2.5 GPa: Implications for Fe3+ content of MORB and OIB source mantle. Geochimica et Cosmochimica Acta.

Seitz, H. M., Altherr, R., & Ludwig, T. (1999). Partitioning of transition elements between orthopyroxene and clinopyroxene in peridotitic and websteritic xenoliths: new empirical geothermometers. Geochimica et Cosmochimica Acta, 63(23-24), 3967-3982.

Shervais, J. W., Taylor, L. A., Lugmair, G. W., Clayton, R. N., Mayeda, T. K., & Korotev, R. L. (1988). Early Proterozoic oceanic crust and the evolution of subcontinental mantle: Eclogites and related rocks from southern Africa. Geological Society of America Bulletin, 100(3), 411-423.

Stosch, H. G., & Lugmair, G. W. (1990). Geochemistry and evolution of MORB-type eclogites from the Münchberg Massif, southern Germany. Earth and Planetary Science Letters, 99(3), 230-249.

Taylor, L. A., & Neal, C. R. (1989). Eclogites with oceanic crustal and mantle signatures from the Bellsbank kimberlite, South Africa, Part I: mineralogy, petrography, and whole rock chemistry. The Journal of Geology, 97(5), 551-567.

Walter, M. J. (1998). Melting of garnet peridotite and the origin of komatiite and depleted lithosphere. Journal of Petrology 39, 29-60.

Wijbrans, C. H., Klemme, S., Berndt, J., & Vollmer, C. (2015). Experimental determination of trace element partition coefficients between spinel and silicate melt: the influence of chemical composition and oxygen fugacity. Contributions to Mineralogy and Petrology, 169(4), 1-33.

Supplementary figures

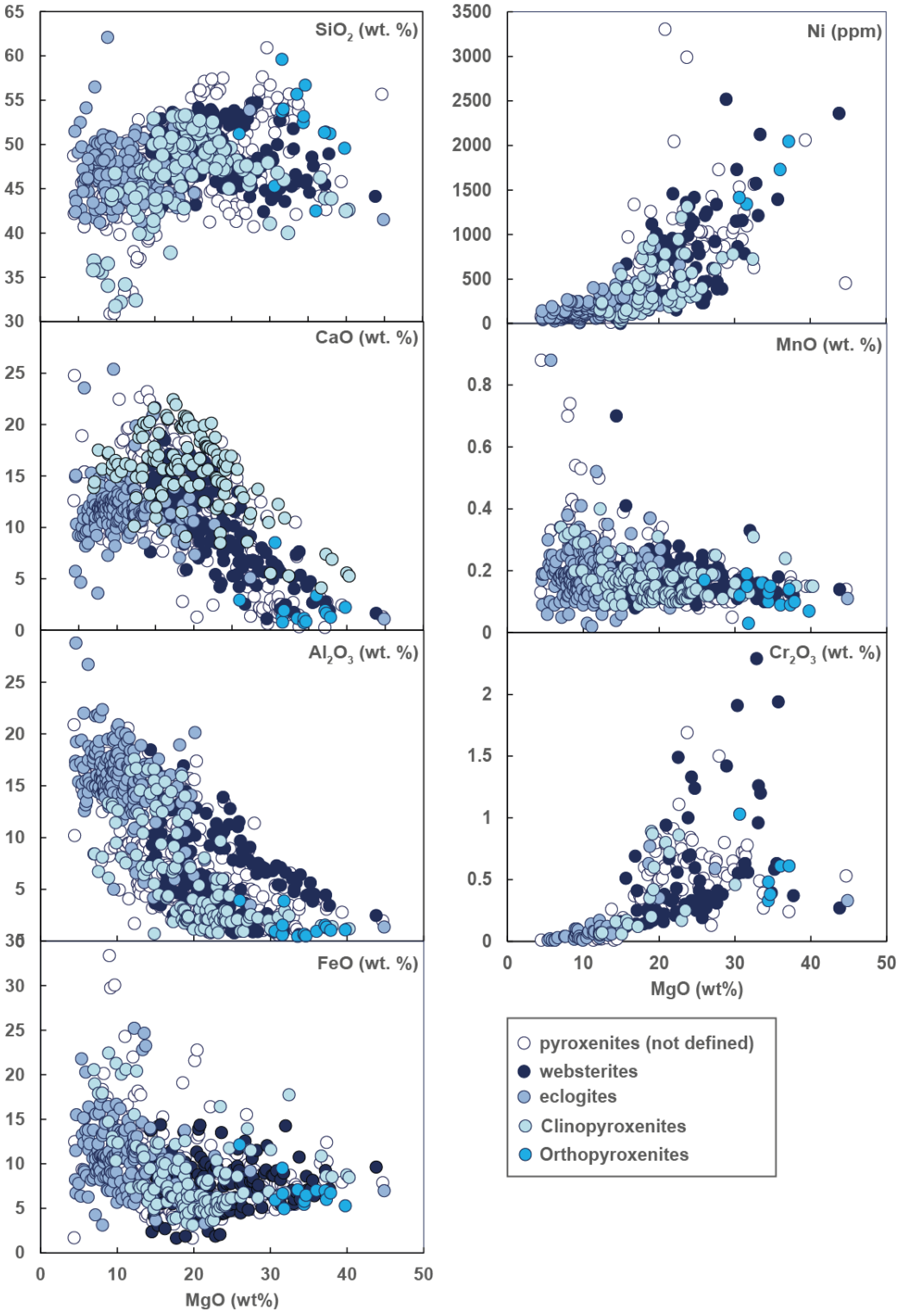

Figure S1. Bulk rock compositions for pyroxenites from the literature. Bulk compositions were download from the EarthChem database (see criteria in the main text) and also compiled from Beard *et al.,* 1992; Bernar-Griffths & Cornichet, 1985; Hills & Haggertly, 1989; Miller *et al.,* 1988; Shervais *et al.,* 1988; Stosch & Lugmair, 1990; Taylor & Neal, 1989.

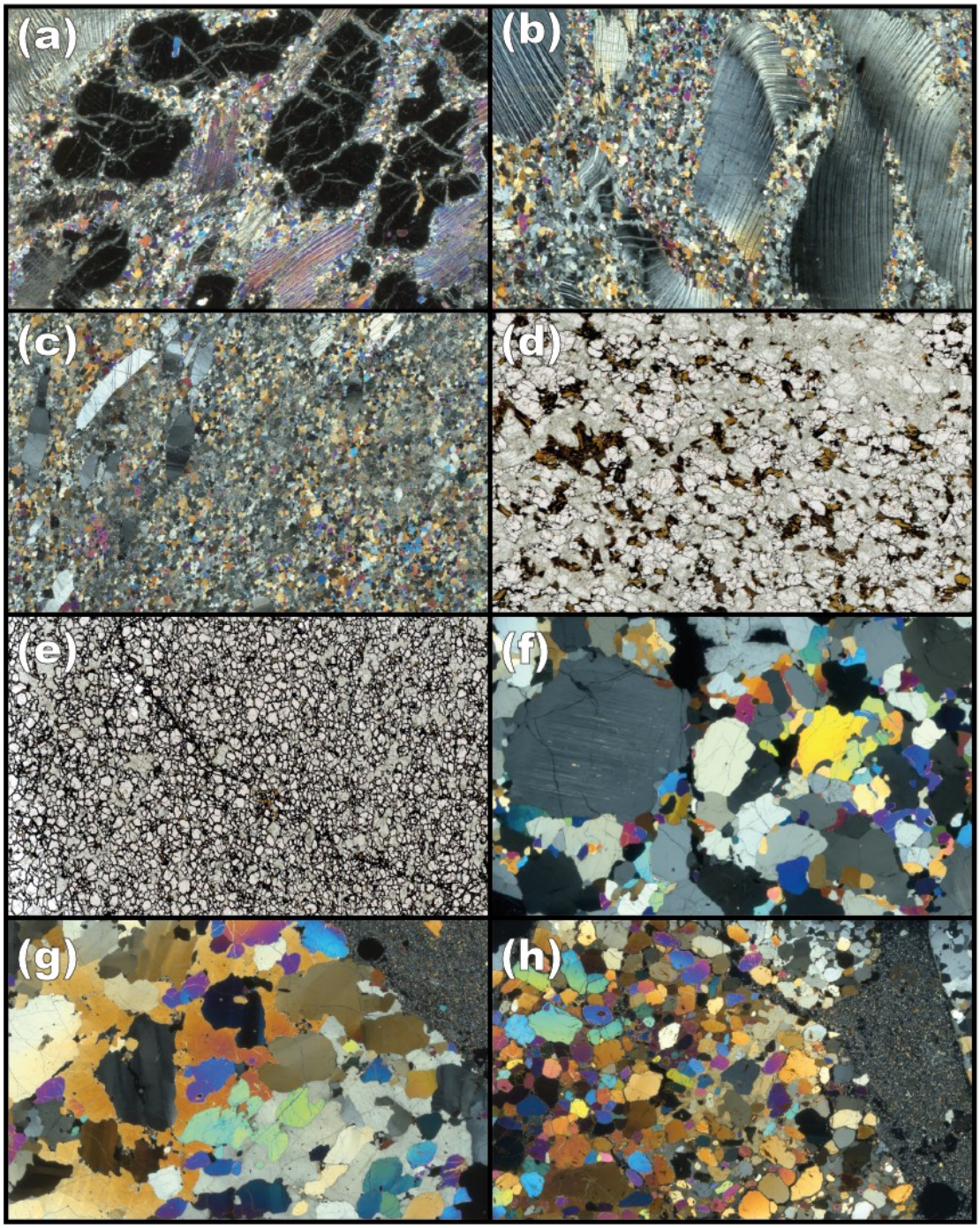

Figure S2. Thin section scans in plane (PPL) or crossed-polarized light (XPL) of selected samples in this study. (a) BB-C-P (XPL); (b) BB-OP-1 (XPL); (c) BB-COR; (d) CV-4 (PPL); (e) CV-16 (PPL); (f) SC2 (XPL); (g) SC3-2 (XPL); (h) SC5-A. The field of view for all samples is approximatively 35*22mm.

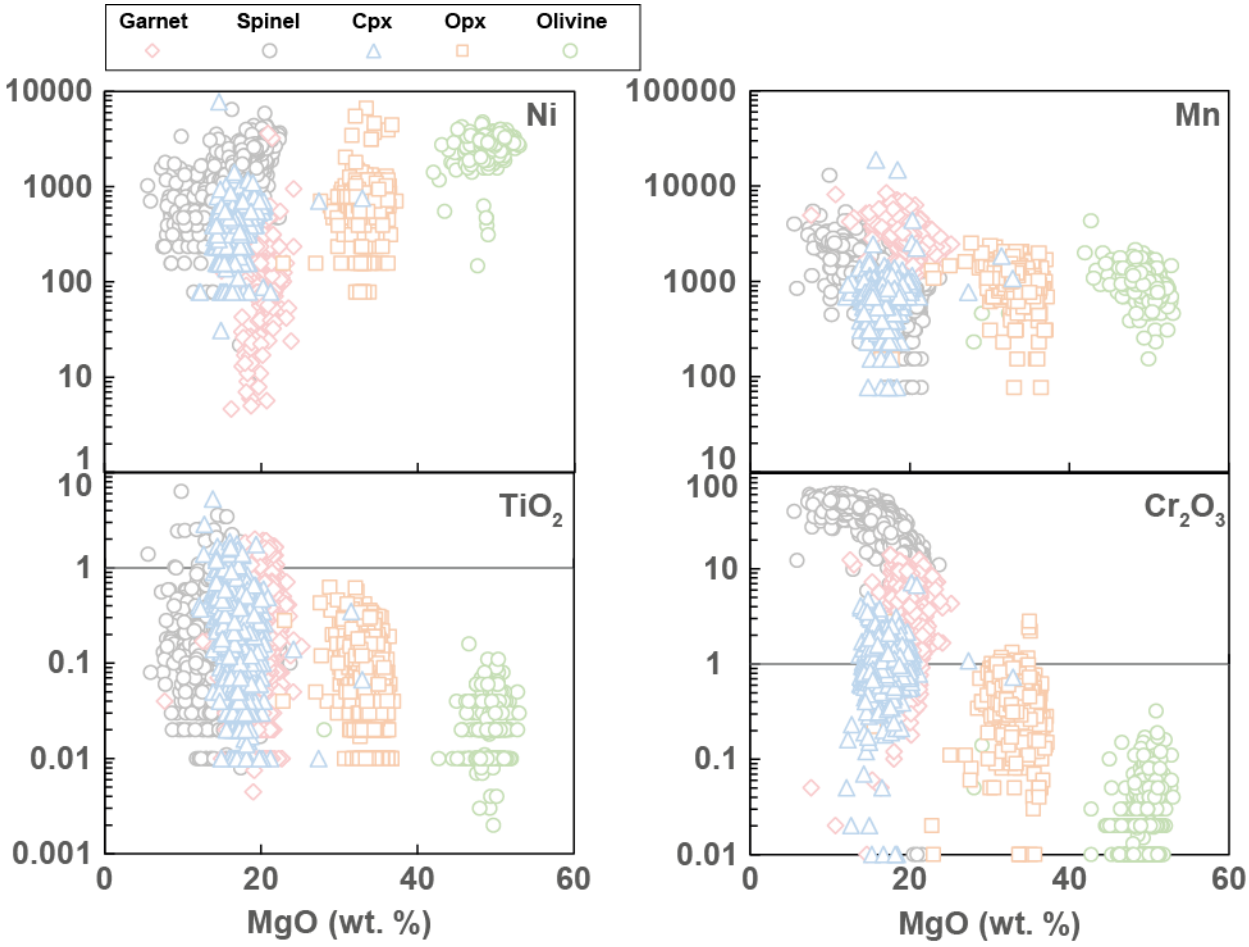

Figure S3. Ni, Mn, TiO_2 and Cr_2O_3 concentrations (oxides are in wt.%, elements are in ppm) as a function of MgO content in olivine, clinopyroxenes, orthopyroxenes, garnet and spinels in peridotites.

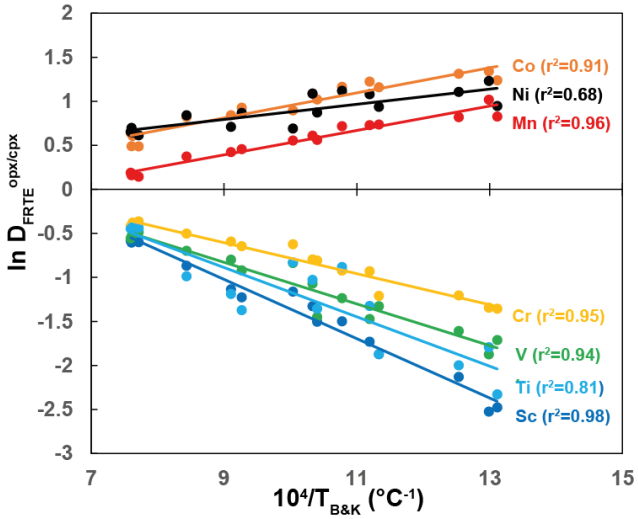

Figure S4. FRTE partition coefficients between opx and cpx as a function of the calculated reciprocal temperatures (Brey & Köhler, 1990) of xenoliths assuming *P* = 1.5 GPa for the set of xenoliths studied by Seitz *et al.* (1999).

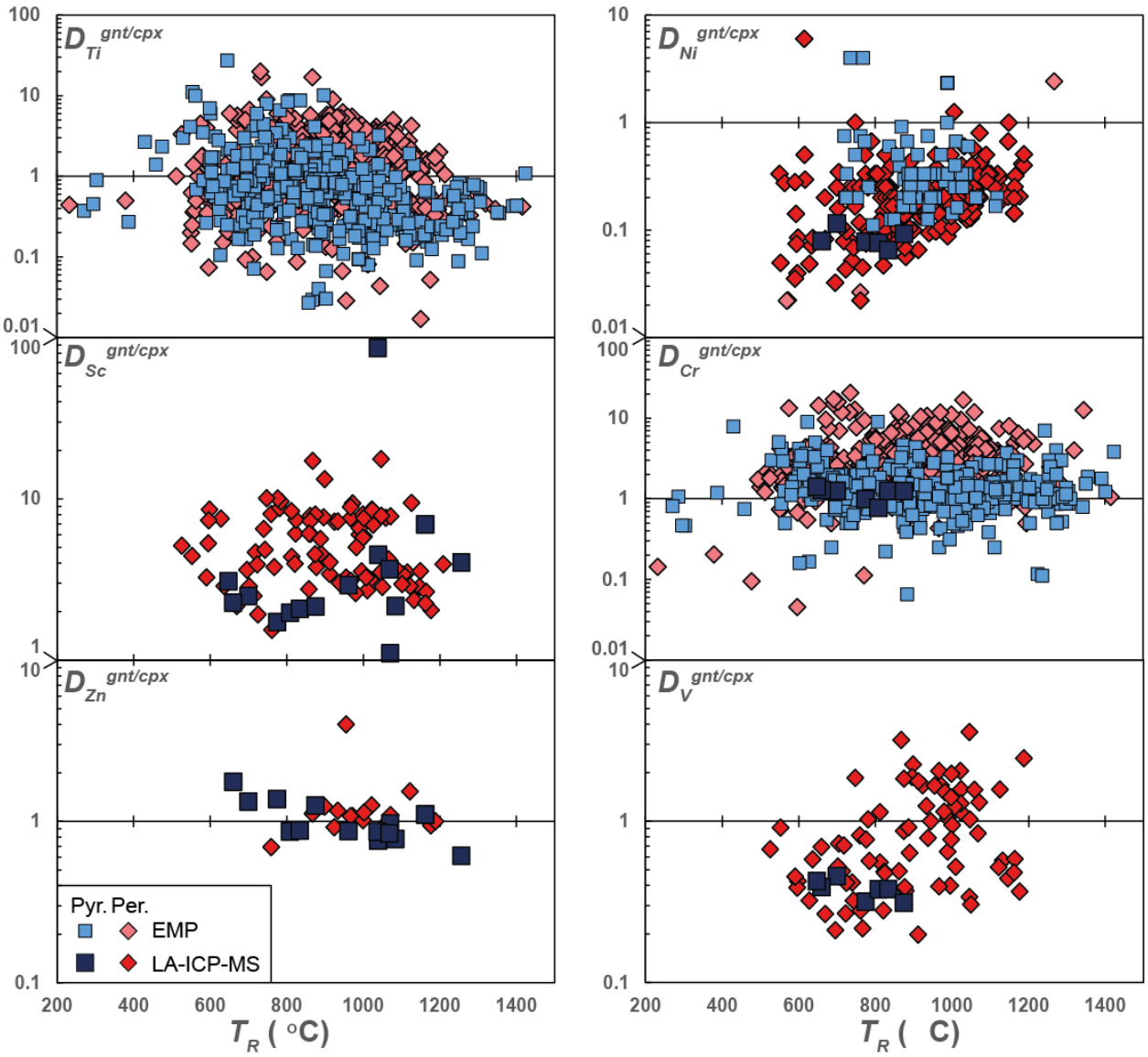

Figure S5. Ti, Ni, Sc, Cr, Zn and V partition coefficients between grt and cpx as a function of Ravna (2000)'s cpx-gnt temperatures in pyroxenite (pyr.) and peridotite (per.) assemblages. Pressure is assumed equal to 1.5 GPa for both datasets.

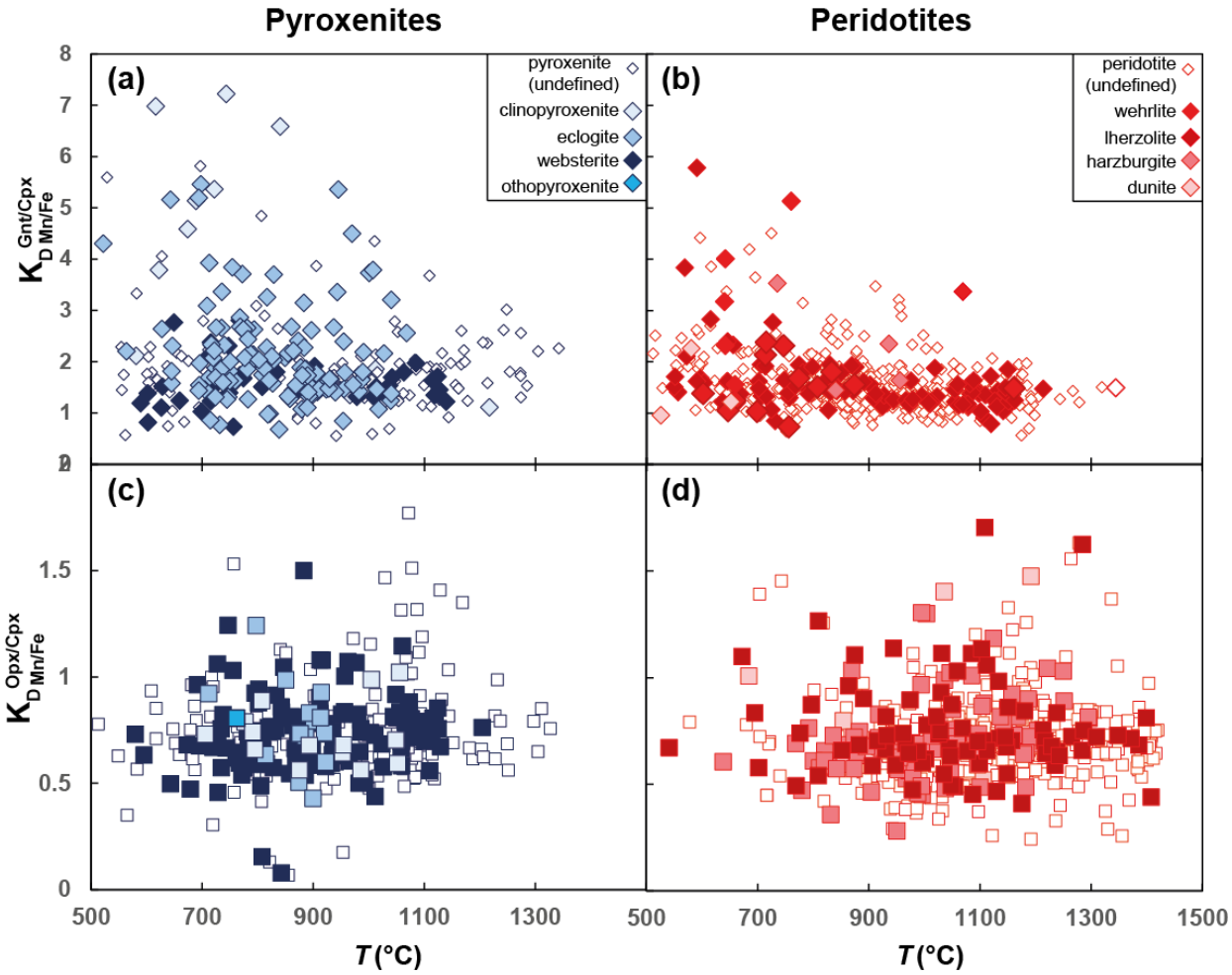

Figure S6. Mn-Fe exchange coefficients between garnet (a-b) or opx (c-d) and cpx as a function of temperature for the pyroxenite (left) and the peridotite (right) datasets. Temperatures are calculated with Ravna's Gnt-Cpx thermometer (2000) in (a-b) and Brey & Köhler's Opx-Cpx thermometer (1990) in (c-d).

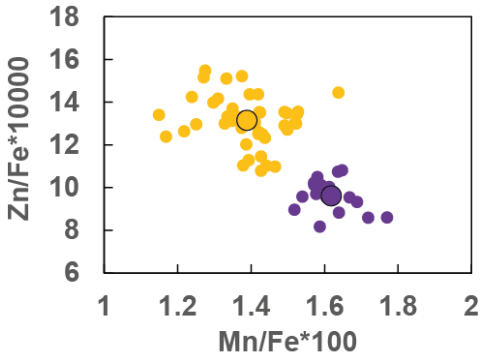

Figure S7. Zn/Fe and Mn/Fe ratios reported for the Iceland basalt suite (purple; Eason *et al.,* 2015) and the Samoa basalt suite (yellow; Beunon *et al.,* 2020). The larger symbols are the average melt ratios used in the inverse modelling calculations (section 6 in the main manuscript).

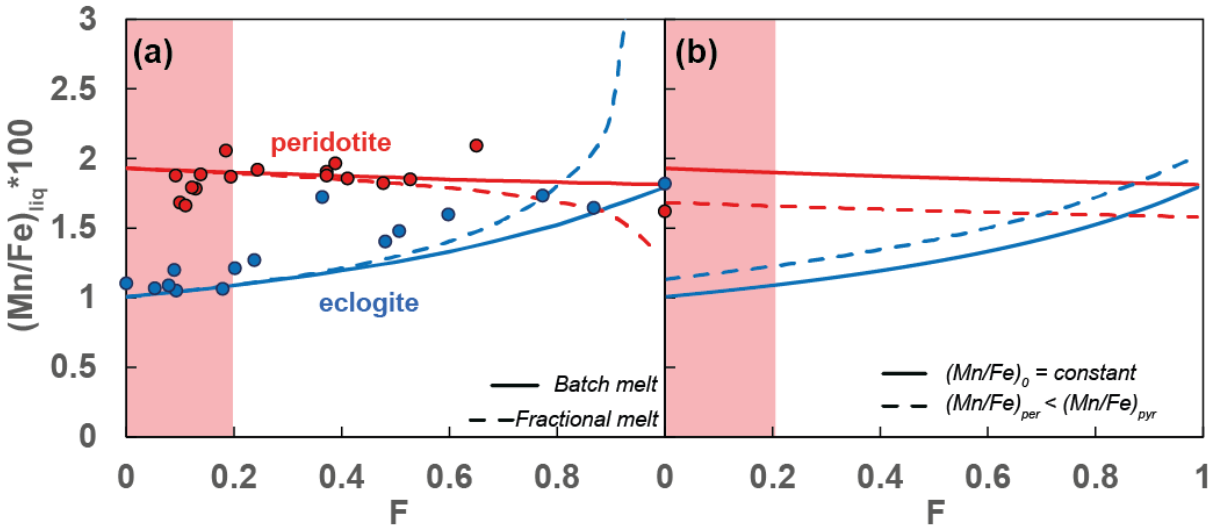

Figure S8. Mn/Fe *100 values in the melts produced by peridotite (red) and eclogite (blue) as a function of the melt fraction (F). **(a)** compares the ratios obtained using the batch melting (solid line) and the fractional melting (dashed lines), with the experimental melts from the eclogite G2 (Pertermann & Hirschmann, 2003a) and the peridotite KR4003 (Walter, 1998). **(b)** compares the results obtained with the batch melting equation but assuming either a constant $(Mn/Fe)_0$ for both lithologies (solid line) or different $(Mn/Fe)_0$ for each lithology. The red shading marks the range of F (0 to 20%).

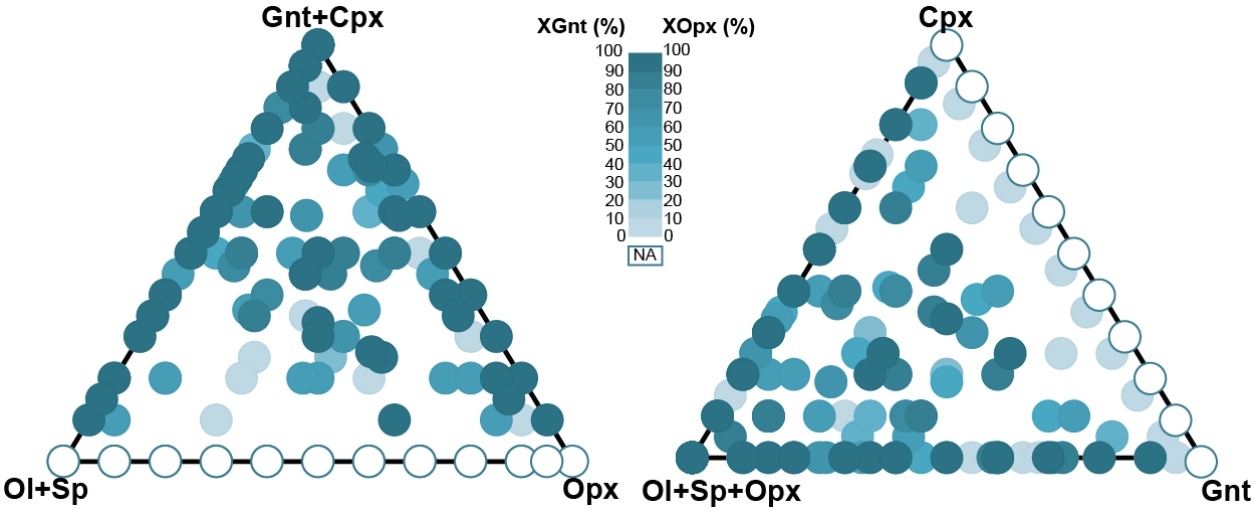

Figure S9. Individual modal mineralogy used as input in the 200 runs (see section 5 for details). XGnt = Gnt/(Gnt+Cpx); XOpx = Opx/(Opx+Ol+Sp). "NA" ratios are for input run without garnet and cpx on the left panel and without opx, olivine and sp on the right panel.

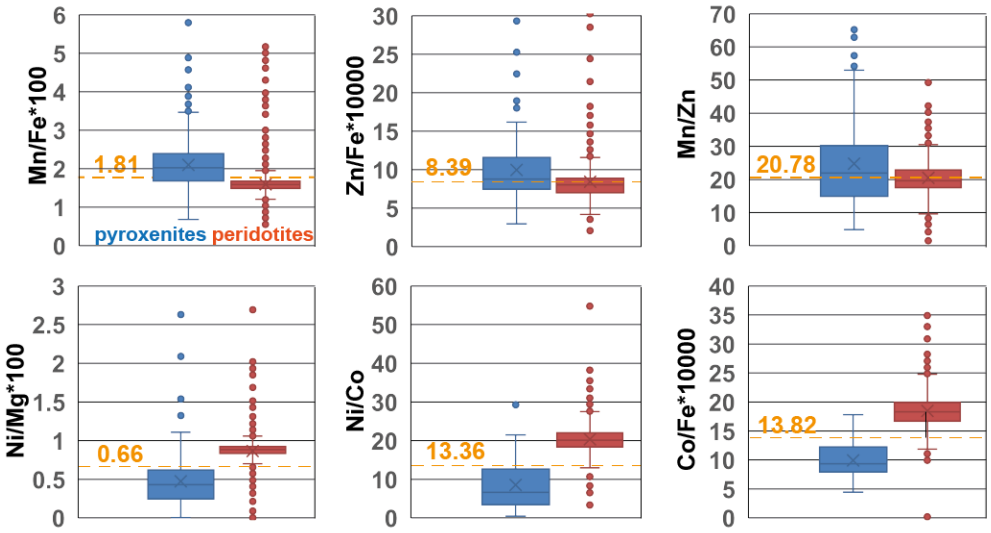

Figure S10. Box plot of FRTE ratios for the pyroxenite database (blue) and the peridotite database (red). Within each box, horizontal lines denote median values; boxes extend from the 25th to the 75th percentile of each group's distribution of values; vertical extending lines denote adjacent values (i.e., the most extreme values within 1.5 interquartile range of the 25th and 75th percentile of each group); dots denote observations outside the range of adjacent values. The orange dashed line represents the average value of the medians from both datasets.

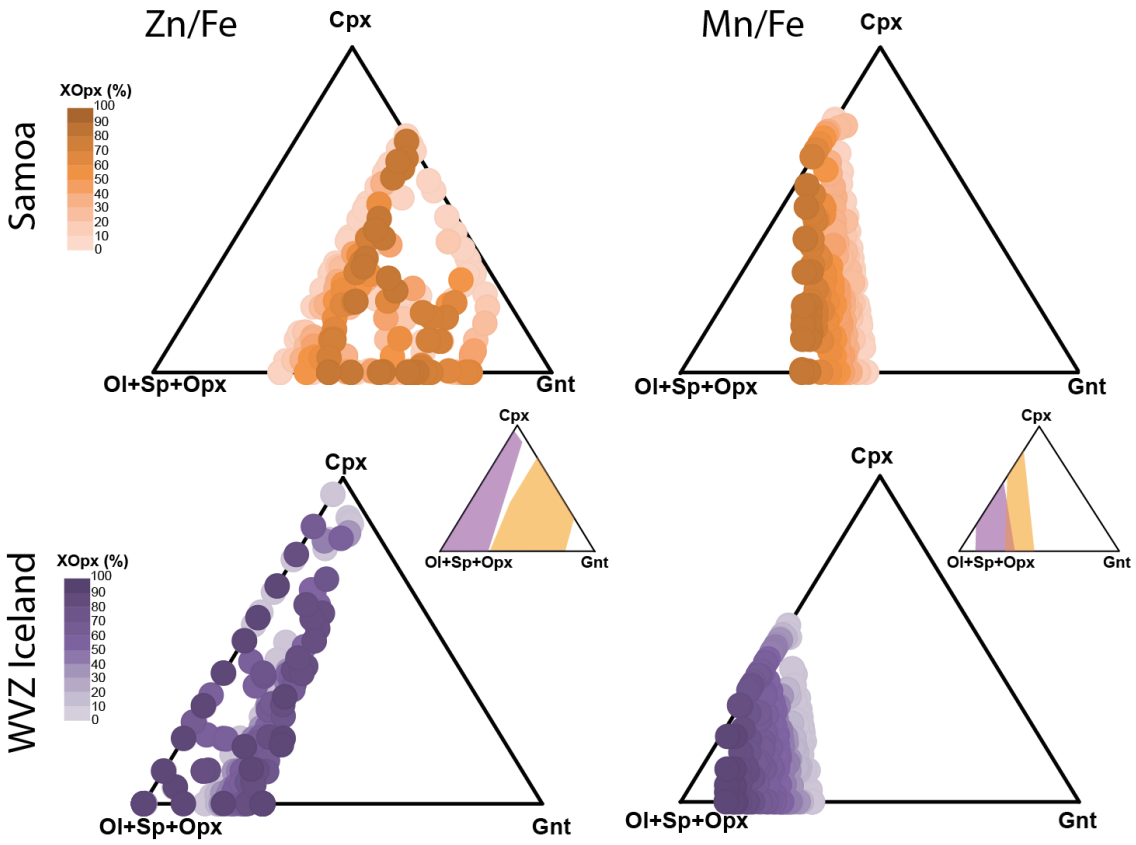

Figure S11. Batch melting model results: output modal source proportions reproducing either the average Zn/Fe ratios (left column) or the Mn/Fe ratios (right column) of the basalt suites from Samoa (top) and the WVZ in Iceland (bottom). The small triangles illustrate the potential overlap between the two basaltic series for a given ratio. XOpx = Opx/(Opx+Ol+Sp).

Table S3. Modal proportions of the xenoliths analyzed in this study

	BB-C-P	BB-OP	BB-COR	CV-4	CV-16	SC2-1	SC4-w	SC3-1	SC3-2	SC5-A
Lithology*	gnt web	web	cpxite	amp arclogite	arclogite	ol opxite	ol web	ol web	ol web	ol cpxite
olivine						22	10	55		58.5
cpx	54	28	87	45	36	4	42	55	58	39
opx	12	72				73	47	41.6	41	
garnet	30		2.5	40	62					
amph	4			15	2			3		
corundum			10							
spinel			0.5			1	1	0.4	1	2.5

Mineral proportions were determined by point-counting. See Supplementary Text S2.1.

Table S7. Modal proportions used for the peridotite (per) and the pyroxenite (pyr) in the bilithological models (section 5.3)

	run #1*				**run #2**			
	WVZ		**Samoa**		**WVZ**		**Samoa**	
	per	pyr	per	pyr	per	pyr	per	pyr
ol	53.1	0	53.1	0	50	19	63	0
opx	27.3	0	27.3	0	22.5	35	24.3	0
cpx	17.7	82	17.7	82	24.5	29	10.8	50
gnt	1.9	18	1.9	18	0	20	1.9	50
sp	0		0		3	0	0	0
Mn/Fe%[a]	34		67		49		64	
Zn/Fe%[b]	<0		>100		49		64	

* in Run #1, we consider the same lithologies in both mantle sources. In run #2, output of the calculations for the bulk mineralogy of the mantle source (section 5.2) are taken into account. See section 5 for details.

[a] % of pyroxenite contributing to the magma calculated using the Mn/Fe ratio

[a] % of pyroxenite contributing to the magma calculated using the Mn/Fe ratio